"Characterising the skull base in craniofacial microsomia using principal component analysis."

Author list: Sontje-Chiao **Schaal**, MD[1]; Clifford **Ruff**, MSc[2]; Britt I. **Pluijmers,** MD, DDS[3]; Erwin

Pauws, BSc, PhD, AFHEA[4]; Caspar W.N. **Looman**, MSc[5]; Maarten J. **Koudstaal**, MD, DMD, PhD [1,2];

David J. **Dunaway**, MBChB, FDSRCS, FRCS(plast)[1]

1. The Craniofacial Unit, Great Ormond Street Hospital Institute of Child Health, London, The United

Kingdom.

2. Medical Physics Department, University College London, London, The United Kingdom.

3. The Dutch craniofacial center department of oral and maxillofacial surgery, Erasmus MC, Rotterdam,

The Netherlands.

4. Department of developmental Biology & Cancer Programme, UCL Great Ormond Street Hospital

Institute of Child Health, London, The United Kingdom.

5. Department of public health, Erasmus MC, Rotterdam, The Netherlands

Corresponding author:

Sontje-Chiao Schaal, MD

Erasmus MC

The Dutch craniofacial center dept. of oral and maxillofacial surgery

's Gravendijkwal 230

3015 CE Rotterdam, The Netherlands

sontjeschaal@gmail.com or s.schaal@erasmusmc.nl.

Keywords: Craniofacial microsomia, Skull base, Principal Component analysis, Facial asymmetry.

Short Running head: Characterising the skull base

ABSTRACT

To compare and determine the anatomical difference in skull base between the affected and non-affected side within craniofacial microsomia (CFM) and to the normal population. 3DCT scans of 13 unilateral CFM and 19 normal paediatric patients within age range 7-12 years were manually landmarked with reliable homologous landmarks. Principal component analysis (PCA), as part of a point distribution model (PDM) was used to analyse the variability within the normal and preoperative CFM group. By analysing the differences in the principal components calculated for the two groups, a model was created to describe the differences between the CFM group and normal age-matched controls. PDM's were also used to describe the shape changes in skull base between the cohorts and validated our model. Using thin-plate splines (TPS's) as a means of interpolation, movies were created to visualize the transformation from a CFM skull into a normal skull, and to display the variability in shape changes within the groups themselves. The skull base of the CFM had a significant asymmetry. Anatomical areas around the glenoid fossa and mastoid process showed the most asymmetry and restriction of growth, suggesting pathogenesis involvement of 1st and 2nd pharyngeal.

INTRODUCTION

Craniofacial microsomia (CFM) is the second most common congenital craniofacial anomaly after cleft

lip and palate.[1] The prevalence is between 1 in 3000 to 1 in 5000 live births. [2-4] CFM has a heterogeneous

presentation, mainly characterised by hypoplasia in the auricular, mandibular and maxillary anatomical

region.[5-8] Many of the clinical features originate from structures that arise from the first and second

pharyngeal arches, thus involvement of the adjacent anatomical structures might also occur within this

congenital craniofacial condition.[4,9]

The aetiology or underlying cause of CFM remains a subject of discussion in the literature. The

different theories consist of a sporadic event, disturbed migration of cranial neural crest cell, to a

hereditary role in genetics.[10,11,12, 13, 14]Another hypothesis consist of stapedial artery disruption causing

ischaemic necrosis to anatomical features in the first and second pharyngeal arches.[15]

The variety in phenotypic presentation of CFM may be due to the wide variety of structures that

arise from the first and second pharyngeal arches.[18,19,20,21]. The Pruzansky-Kaban classification is the most

commonly known used classification system to describe mandibular deformity in CFM and was used for

this study. [16,17] The skull base is in close relation with the facial skeleton and the morphology of the skull

base has an influence on the facial asymmetry.[22,23] CFM is mainly characterized by the facial asymmetry

and thus far only one study has evaluated the skull base. This study concludes that the skull base axis is

not deviated compared to those of the age-matched controls and that there exists little difference in

morphologic measurements with increasing severity of CFM.[24]

The data contained within conventional 3DCT scans can be utilised in mathematical techniques

such as geometric morphometrics to analyse complex shapes. In our study principal component analysis

(PCA) is performed on manually landmarked 3DCT scans to identify the global complex shape of

different skulls. The difference between the affected and unaffected population can then be visualized and

described. This technique has been successfully used for analysing Apert syndrome and Crouzon-Pfeiffer

syndrome.[25-27]

The aim of this study is to determine the anatomical difference in skull base between the affected

and non-affected side in CFM and between the CFM and normal population.

MATERIAL AND METHODS

Data collection

The inclusion criteria were patients diagnosed with unilateral CFM, who had suitable preoperative 3DCT

scans available, ages between 7 and 12 without any history of craniofacial skeletal surgery. Patients were

classified with the Pruzansky-Kaban system, type 1-2B were included. (Table 1 and 2) Patients classified

as Pruzansky-Kaban type 3 were excluded since essential anatomical features are missing making them

inappropriate for our type of analysis. Bilateral CFM patients were also excluded, since the affected sides

were nullifying each other during the analysing. The inclusion criteria for the control group were patients

with unaffected craniofacial skeleton, aged between 7-12 years. (Table 3) After incorporating the

inclusion criteria, a total of 13 unilateral CFM patients (8 right- and 5 left-sided CFM) with preoperative

3DCT scans were available for analysis. 19 normal patients were included as a control group.

At Great Ormond Street Hospital (GOSH) the 3DCT scans were taken by using a 16-slice

Siemens Somatom Sensation spiral CT-scanner set to 0.75 collimation (Siemens Medical Solutions,

Malvern, PA, USA). Patients at Erasmus MC were scanned by using a 6-slice Siemens Spiral CT scanner

(Emotion 6, Siemens, Munich, Germany) with a fixed slice thickness of 0.8 mm. All scans were saved as

Digital Imaging and Communications in Medicine (DICOM) files and were converted into a University

College London (UCL) proprietary format. The formats were loaded into a 3D voxel-imaging software

(Robins 3D, 2013). For all 3DCT scans a Hounsfield between 223 and 431 was chosen as the threshold

for data imaging the bony tissue surface. For accurately placement of the landmarks on the skull base

surface, the mandible and the top cranium had been separated and segmented off from the rest of the

craniofacial skeleton.

Landmarks

An accurate and reliable set of homologous landmarks had to be determined to compare normal and CFM

patient scans. To increase the reliability and repeatability of the landmarks, they were placed on

anatomical points of the skull base. An iterative process was used to test different landmark sets and to

determine which distribution of landmarks best described the morphology of the skull base in normal and

CFM patients. The landmarks were mainly placed around the anterior and middle skull base, due to

surgical interest and expected affected areas of CFM. (Figure 1 and 2) Therefore, a smaller number of

landmarks was located on the posterior skull base. It was important that the set of landmarks used

captured all key shape features of the skull base. The landmark set used was developed and validated

using thin-plate spline warps (TPS) and a visualisation technique using false colours to represent

differences between two skull shapes. A random normal scan was chosen and TPS warped to the

landmark-coordinates of another randomly chosen normal target scan, this process brought the two sets of

landmarks into alignment. Thin plate splines were used to interpolate between the landmarks in the

warping process. Colour coded images were then generated to show the remaining differences between

the two scans, with the colour at each point on the image representing the distance of that point on the

scan to the closest point on the target scan. (Figure 3) If the landmarks were sufficiently distributed to

capture the surface detail between landmarks, little to no difference would appear on the color maps and

areas that were poorly described by the chosen landmarks would show up as different colours. For the

CFM population, additional TPS warps were made to visualize colour maps. This process was repeated

on the CFM scans to ensure that the chosen landmarks also described the CFM population taking into

account any further shape differences introduced by the anomaly (Figure 4). The final set used consisted

of 51 homologous landmarks that were located on all normal and CFM scans (Table 4).

Data analysis

To determine the repeatability of the landmarks, a normal skull and a CFM skull were chosen at random

and landmarked in ten times with at least 48 hours between sessions to reduce memory bias. The means

and the standard deviations (SD) were then calculated to demonstrate the reproducibility of the

landmarking process, the results are shown in table 4. In normal and CFM bony tissue a SD less than 2

mm was determined acceptable and less than 1 mm accurate.[28,29]

Left-sided CFM patients were mirrored to create right-sided deformity for shape analysing the

variety in side deformity within CFM as one uniform group. The mirroring of unilateral CFM was done

under the assumption that the affected side either on the right or left were comparable. The landmark data

was then analysed using a Point Distribution Model (PDM) software package. The PDM was a form of

statistical shape or morphometric analysis whose function was to capture the statistics of variation seen in

a group of related shapes. It was a form of multivariate analysis that analysed the input or training shapes

in a holistic manner by looking not just at how each point varied in isolation, but how each point on the

shape co-varied with every other point. The PDM accomplished this by representing each of the training

shapes by a set of homologous landmarks, from which a mean shape was calculated. Each shape in the

training set was then expressed as a difference from this mean, and a table of how each point co-varied

with respect to every other point, was calculated for each shape, and then summed over all of the shapes

in the training set to form a covariance matrix that represented how each landmark tended to vary in

relation to every other landmark in the training set taken as a whole.[30,31]

Eigenvector analysis was then applied to this covariance matrix to yield a set of eigenvectors and

eigenvalues, where each eigenvector represents a way, or direction, in which the landmarks tended to vary

as a group, and the associated eigenvalue represented how much of this variation was present in the

training set, or its variance. Each eigenvector could be thought of as a "mode of variation" or way in

which the overall shape varied within the training set. Principal Component Analysis (PCA) could then be

applied by ordering the eigenvectors, or modes of variation, in descending order of their eigenvalues, and

retaining only the modes with the highest values, which represented the modes of variation that accounted

for most of the variation seen in the training shapes. The final model consisted of a mean shape and a set

of modes (or principal components) of variation and their relative importance (the eigenvalues) in

describing the variation seen in the training set. The modes of variation could be visualised by applying

weighted amounts of the eigenvalues (i.e. +/- 2 SD) of the eigenvectors to the mean shape and generating

a movie of the transformation between the shapes thus generated, using TPS as a means of interpolation

between the landmarked points.

In summary, the method used was to first generate a set of homologous landmarks, that described

the areas of interest in the skull base which were validated as sufficient for the task by warping and

colourmap comparisons (Figures 3 and 4). The resulting set of 51 landmarks were then considered to

represent the shape of the important area of interest in the skull base as a whole and were located on all

the normal and CFM scans. PDM's were then generated from these landmarks on both the normal and

CFM sets individually, and movies of the modes of variation produced were generated. Finally, a joint

model was built in an attempt to cancel out the normal modes of variation from the CFM model to leave

only the differences between the two training sets, and a movie of the principal component of this

difference applied to the mean shape of the normal was generated.

Linear measurements

After analysing the anatomical changes seen in the PDM model, linear measurements were taken using

Robins 3D. Additional landmarks were chosen based on anatomical and surgical interest as well as

defined by Paliga et al, to measure the intermediate distances. The tuberculum sellae was chosen as the

reference point for specific landmark measurements, being at a central position in the skull base. Fourteen

measurements were performed on the affected and non-affected sides of CFM and normal skull base.

Measurements were compared within and between these groups.

Difference in angle and cranial base length were statistically tested with a simple ANOVA-test.

For testing the differences between the affected side of CFM, the unaffected side of CFM and the normal

cohort, a multilevel analysis was performed with the child as random effect. Meaning that the analysis

between sides within the children was compatible to a paired t-test. By adding a normal cohort to the

dataset, the dependencies within the cohort were accounted for. For all analyses, statistical significance

was defined as P-value < 0.05.

RESULTS

All patients with CFM were clinically identified at Great Ormond Street Hospital, London, United

Kingdom. The control group consisted of epileptic patients from GOSH and patients with other medical

conditions scanned at Erasmus MC, Rotterdam, The Netherlands.

Landmark intra-observer reliability

The standard deviation (SD) for all 51 homologous landmarks was calculated. (Table 4) All landmarks

were below a SD value of 2,4 mm.

Normal cohort

5 out of 51 landmarks had a SD between 1mm and 1,4mm. 46 landmarks had the SD threshold of < 1

mm. The placement of the landmarks was for 90% highly accurate and 100% within the 2mm limit.

Craniofacial microsomia cohort

2 out of the 51 landmarks were outside the limit of 2 mm. The SD of 5 landmarks were between 1 mm

and 2 mm. 44 landmarks were < 1 mm, therefore 86% of the landmarks were accurate. 96% were within

the 2mm threshold.

Landmarks placed on distinguishable anatomical features for example foramen ovale were easily

recognized and thus accurately placed. Due to anatomical missing characteristics of CFM, certain

landmarks such as the porion were more difficult to place than on the normal population. Points described

on maximum or minimum curvature were slightly less reproducible.

Variation within the cohorts

PDM's were generated within the normal and preoperative unilateral CFM group to define the variability.

The first three modes of variations were modelled and visualized through TPS movies.

The first mode of variation in the normal populations showed allometric growth of the skull base.

The second mode mainly showed normal widening in the sphenoid and temporal bone of the skull base.

There was a slight asymmetry even within the normal population. The third mode of variation visualized

a combination in variation in length and width within the normal cohort. (see videos, Supplementary

Digital Material 1-3, which demonstrates the first three modes of variation in normal)

In the first mode of variation of the unilateral CFM group showed allometric growth. The second

principal component showed the variability in severity of CFM. Variation in orientation of the temporal,

partially the sphenoid and the orbital bone was displayed on the affected side, especially around the

foramen jugular, foramen ovale, mandibular process, styloid process and occipital condyl. On the affected

side a twist of the temporal bone into anteromedial direction was seen. Little variation in displacement

was seen in the mastoid process. The unaffected side had a width decrease and a length increase. The

third mode demonstrated reduced width on the affected side. The foramen ovale moved medially. The

contralateral side had shape changes consistent to normal allometric growth. Therefore, the palatine bone

partially overrode the midline of the skull base to the affected side. (see videos, Supplementary Digital

Material 4-6, which demonstrates the first three modes of variation in CFM)

Variation between the cohorts

To illustrate the shape changes between the normal and preoperative CFM skulls, a joint model was built

in an attempt to cancel out the normal variation from the CFM group. The resulting principal component

of the difference model was applied to the normal mean and movies were made to visualize any shape

changes from a normal skull to a CFM skull.

The temporal bone on the affected side of a normal skull changed in medial direction and

shortened in length to transform into a CFM skull. The mandibular fossa and mastoid process moved

towards each other. There was also a medial and cranial displacement of the external acoustic meatus,

process styloid, foramen jugular and petrous part of the temporal bone. A posterolateral displacement of

the maxilla and the palatine bone were shown. Overall the midline of the skull base showed a slight twist

to the affected side. Thus, the relevant anatomical features on the temporal and sphenoid bone of a CFM

skull moved closer together and the distance within became smaller than on a normal skull. (see video,

Supplementary Digital Material 7, which demonstrates the skull from normal to CFM)

Linear measurements

For the angle, anterior part and total length of the skull base no significant difference was shown between

the CFM and normal cohort. (Table 5 and 6) 8 out of 14 measurements varied significantly between the

affected and unaffected CFM side. (Table 7) Between the affected CFM-side and normal, 10 out of 14

landmark measurements showed significantly difference. (Table 8) A comparison of the unaffected CFM-

side to the normal cohort indicated no significant difference for 12 out of 14 measurements. Exceptions

were the hypoglossal canal to tuberculum sellae and the temporal bone to tuberculum sellae, which varied

significantly.

DISCUSSION

In comparison to studies using angulation and craniometrics measurements, PDM's account for all the variability present in the data, thus it is possible to objectively describe the normal and CFM shape changes.

Recent study by Paliga et al. demonstrated no cranial base axis deviation and little difference in endocranial morphologic measurements. Based on their results the authors suggested that the skull base seems to be spared in CFM and pathophysiology of Poswillo's stapedial artery insult hypothesis in the restriction of abnormalities to derivatives of the 1st and 2nd pharyngeal arches in this area.[15,16,24] A significant part of the skull base is derived from derivatives of the 1st and 2nd arches (squamous temporal bone, glenoid fossa, root of zygoma, spine of sphenoid and styloid process). It would be surprising to find these structures unaffected if 1st and 2nd arch involvement in the pathogenesis CFM is correct. Closer examination of the landmark set used by Paliga et al shows that none of these landmarks are placed on 1st and 2nd arch derivatives and so it is not surprising that their study showed no significant asymmetry.

In this study, we have generated and validated a set of 51 landmarks that describe the most important feature of the cranial and caudal side of the skull base. Landmarks compatible with the Paliga study are included along with more widely distributed landmarks particularly including the temporal bone. PDM's show that landmarks on the temporal bone and surrounding structures are antero-medially

displaced and parts of the temporal bone are rotated and vertically displaced leading to a complex

deformity and asymmetry. The rotational deformity becomes more marked with the severity of deformity.

All modes of variation show minor changes in the "unaffected side". It is likely that these

changes are a compensatory response to the deformation of the skull base on the affected side, but also

possible that they may represent a minor direct influence of the pathological process on this part of the

skull base (i.e. the CFM process is to some degree bilateral in all cases).

The linear skull base measurements were used to objectify, characterise and analyse the visual

changes seen in the PDM model. Furthermore, the measurements were taken to locate the differences in

specific anatomical areas within the CFM skull base and to compare this to the normal cohort. As

indicated in the study by Paliga, our results show no significant difference in cranial base angle, anterior

length and total length between the CFM and normal cohort. Our study demonstrated, the posterior

cranial base length, measured from the tuberculum sellae to opisthion, does display significant variance

which can be influenced by the small population numbers. This area is a considerable distance from any

1st and 2nd pharyngeal arch derivatives and can possibly not be explained by this arch theory of

pathogenesis.

Additionally, within the CFM skull base there are significant differences between the affected and

unaffected sides (8 out of 14 measurements), most notably in the middle and posterior cranial fossae. The

comparison between the affected CFM-side and age-matched controls also present a significant variance

in almost all linear landmark measurements (10 out of 14 measurements). These differences are most

marked in the mandibular fossa, mastoid process and temporal bone. The unaffected CFM-side does only

significantly vary from the normal cohort on the following anatomical regions the temporal bone to

tuberculum sellae and hypoglossal canal to tuberculum sellae. These anatomical features are also

significantly different in affected and unaffected sides within the CFM skull. To summarise, the affected

CFM side differs from the normal whereas the unaffected linear measurements differ slightly. On the

affected side, the most severe asymmetries and differences from normal values are centred around the

glenoid fossa, mastoid process and temporal bone. These findings suggest that there is a severe restriction

of growth within and around derivatives of the pharyngeal arches and it is likely that asymmetries seen

elsewhere in the skull base are deformational changes in areas with normal growth ability but directly

connected to the abnormal area. The linear measurements also imply that the skull base asymmetry can

contribute to the facial asymmetry.

     The results clearly show that the skull base is affected in CFM. Since the facial skeleton is in

direct contact with the skull base, it is apparent that skull base asymmetry contributes to facial asymmetry

in CFM. It is not possible to surgically correct many skull base asymmetries, (e.g. the position of the TMJ

or external auditory meatus) which implies that the actual asymmetry of CFM cannot be fully corrected and must therefore be masked by procedures on areas that can be surgically corrected.

A limitation of this study is the age range 7-12 years. Allometric growth is significant in this age range and this has particularly affected the PDM analysis. Although PDM can help identify changes due to growth, many of the subtle anatomical differences caused by CFM may have been masked.

This study is the first to describe a significant asymmetry of the skull base in CFM. The most significant asymmetries and restriction of growth are centred around the glenoid fossa, mastoid process suggesting involvement of 1st and 2nd pharyngeal arch derivatives in the pathogenesis. Distortion of the skull in this area is complex and is present in the vertical, horizontal and antero-posterior planes associated with a rotation of this part of the skull base. More minor abnormalities are present in other parts of the skull base, and are likely to be due to deformation resulting abnormal growth in the region of the affected temporal bone.

REFERENCES

1. Heike CL, Hing AV, Aspinall CA et al. Clinical care in craniofacial microsomia: a review of current management recommendations and opportunities to advance research. *Am J. Med Genet Part C Semin Med Genet.* 163C:271-282, 2013.

2. Poswillo D. The aetiology and pathogenesis of craniofacial deformity. *Development.* 1988;103(suppl):207-2012.

3. Grabb WC. The first and second branchial arch syndrome. *Plast Reconstr Surg*. 1965;36(5):485-508.

4. Birgfeld C, Heike C. Craniofacial Microsomia. *Seminars in Plastic surgery.* 26, 091-104, 2012.

5. Gougoutas AJ, Singh DJ, Low DW, Bartlett SP. Hemifacial macrosomia: clinical features and pictographic representations of the OMENS classification system. *Plast Reconstr Surg.* 2007; 120:112e-120e.

6. Murray JE, Kaban LB, Mulliken JB. Analysis and treatment of hemifacial macrosomia. *Plast Reconstr Surg*. 1984;74f:186-199.

7. Rune B, Selvik G, Sarnäs KV, Jacobsson S. Growth in hemifacial macrosomia studied with the aid of roentgen stereophotogrammetry and metallic implants. *Cleft Palate J*. 1981 Apr;18(2):128-146.

8. Ongkosuwito EM, Van Neck JW, Wattel E, Van Adrichem LN, Kuijpers-Jagtman AM. Craniofacial

    morphology in unilateral hemifacial microsomia. *Br J Oral Maxillofac Surg.* 2013 Dec;51(8):902-7.

9. Converse JM, Coccaro PJ, Becker M, Wood-Smith D. On hemifacial microsomia. The first and

    second branchial arch syndrome. *Plast Reconstr Surg.* 1973; 51(3):268-279.

10. Taysi K, Marsh JL, Wise DM. Familial hemifacial macrosomia. *Cleft palate J.* 1983 Jan;20(1): 47-

    53.

11. Johnston MC, Bronsky PT. Prenatal craniofacial development: new insights on normal and

    abnormal mechanisms. *Crit Rev Oral Biol Med.* 1995;6:368-422.

12. Tuin AJ, Tahiri Y, Paine KM, Paliga, JT, Taylor JA, Bartlett SP. Clarifying the relationships among

    the different features of the OMENS+ classification in craniofacial microsomia. *Plast Reconstr*

    Surg. 2015;135:149e-156e.

13. Werler MM, Sheehan JE, Hayes C, Mitchell AA, Mulliken JB. Vasoactive exposures, vascular

    events and hemifacial microsomia. *Birth defects res a clin mol teratol.* 2004 Jun; 70(6):389-95.

14. Werler MM, Sheehan JE, Hayes C, Padwa BL, Mitchell AA, Mulliken JB. Demographic and

    reproductive factors associated with hemifacial microsomia. *Cleft Palate Craniofac J.* 2004 Sep;

    41(5): 494-50.

15. Poswillo D. The pathologenesis of the first and second branchial arch syndrome. *Oral Surg.* 35(3):302-28;1973.

16. Pruzansky S. Not all dwarfed mandibles are alike. *Birth Defect Orig Artic Ser.* V,2 (1969);120-9.

17. Kaban LB, Moses MH, Mulliken JB. Correction of hemifacial microsmia in the growing child: a follow-up study. *Cleft Palate J.* 1986;23(Suppl1):50-2.

18. Silvestri A, Natali G, Fadda MT. Dental agenesis in hemifacial microsomia. *Pediatric Dent.* 1996 Jan-Feb; 18(1):48-51.

19. Keogh IJ, Troulis MJ, Monroy AA, Eavey RD, Kaban LB. Isolated microtia as a marker for unsuspected hemifacial microsomia. *Arch Otolaryngol Head Neck Surg.* 2007;133:997-1001.

20. Siebert JW, Longaker MT. Microsurgical correction of facial asymmetry in hemifacial microsomia. Operative Techniques. *Plast Reconstr Surg.* 1994;1;93.

21. Heike CL, Luquetti DV, Hing AV. Craniofacial Microsomia Overview. in: R.A. Pagon, M.P. Adam, H.H. Ardinger, S.E. Wallace, A. Amemiya, L.J. Bean et al, (Eds.) *GeneReviews®.*University of Washington, Seattle; 1993-2016.

22. Choi JW, Ra YS, Hong SH. Use of distraction osteogenesis to change endocranial morphology in unilateral coronal craniosynostosis patients. *Plast Reconstr Surg.* 2010 Sep;126(3):995-1004.

23. Marsh JL, Gado MH, Vannier MW, Stevens WG. Osseous anatomy of unilateral coronal synostosis. *Cleft Palate J.* 1986; 23:87–100.

24. Paliga JT, Tahiri Y, Wink J, Bartlett SP, Taylor JA. Cranial base deviation in hemifacial microsomia by craniometrics analysis. *J Craniofac Surg.* 2015 Jan; 26(1):e61-4.

25. Pluijmers BI, Ponniah AJ, Ruff C, Dunaway D. Using principal component analysis to describe the Apert skull deformity and simulate its correction. *J Plast Reconstr Aesthet Surg.* 2012 Dec;65(12):1750-2.

26. Staal FC, Ponniah AJ, Angullia F, Ruff C, Koudstaal MJ, Dunaway D. Describing Crouzon and Pfeiffer syndrome based on principal component analysis. *J Craniomaxillofac Surg.* 2015 May;43(4):528-36.

27. Crombag GA, Verdoorn MH, Nikkhah D, Ponniah AJ, Ruff, C, Dunaway D. Assessing the corrective effects of facial bipartition distraction in Apert syndrome using geometric morphometrics. *J. Plast Reconstr Aesthet Surg.* 2014 Jun;67(6):e151-61.

28. Farkas LG, Munro IR. *Antropometric facial proportions in Medicine*. Springfield, IL Charles C Thomas 1987.

29. Farkas LG. *Antropometry of the head and face*. 2nd ed. New York, NY Raven Press 1994.

30. Cootes TF, Taylor CJ, Cooper DH, Graham J. Training models of shape from sets of examples.

    Proc. BMVC., Leeds, springer-Verlag. 1992; 9-18.

31. Jolliffe IT, ed. *Principal component analysis, second edition*. New York, United States: Springer;

    2002.

LEGENDS OF TABLE, FIGURES AND SUPPLEMENTARY DIGITAL MATERIAL

Table 1. The distribution of age, gender, disorder and affected side of the CFM population.

Table 2. The distribution in age and Pruzansky-Kaban classification of the CFM population

Table 3. Distribution of age and gender in the normal population

Figure 1. The 51 landmarks placed on a normal skull in caudal and cranial view

Figure 2. The set of 51 landmarks placed on a CFM skull in caudal and cranial view

Figure 3. The 10 mm range color-coded map of the warped normal predicted skull being superimposed to

its actual counterpart. The cranial and caudal views are shown. The green and light blue areas display

sufficiently anatomical correspondence between the two scan

Figure 4. The color-code map in 10 mm range of the warped CFM predicted skull superimposed to its

actual counterpart. The cranial and caudal views are shown. The green and light blue areas display

sufficiently anatomical correspondence between the two scans by the chosen landmarks.

Table 4. Set of 51 landmarks on the skull base used for this study. The fourth and fifth column represents

the intra-observer reliability of each landmark.

Supplementary Digital Material 1. Video that demonstrates the first mode of variation in normal cohort.

Supplementary Digital Material 2. Video that demonstrates the second mode of variation in normal

cohort.

Supplementary Digital Material 3. Video that demonstrates the third mode of variation in normal

cohort.

Supplementary Digital Material 4. Video that demonstrates the first mode of variation in CFM cohort.

Supplementary Digital Material 5. Video that demonstrates the second mode of variation in CFM

cohort.

Supplementary Digital Material 6. Video that demonstrates the third mode of variation in CFM cohort.

Supplementary Digital Material 7. Video that demonstrates the mode of variation from a normal to

CFM skull.

Table 5. The mean and SD of cranial base angle (degrees)

Table 6. The mean and SD of cranial base length (mm)

Table 7. The mean and SD lateral measurements (mm) comparison between the affected and unaffected

side in the CFM group

Table 8. The mean lateral measurements and SD (mm) of the affected and unaffected side in the CFM

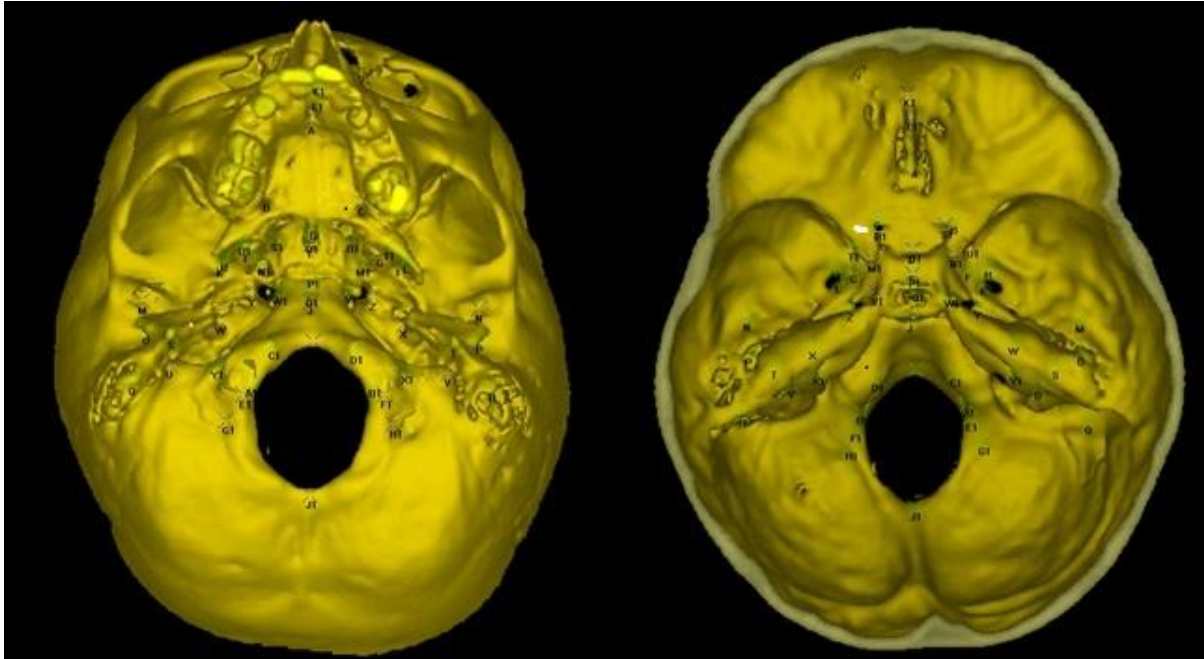group compared to the normal cohort

LIST OF FIGURES

Figure 1

Figure 1 *The 51 landmarks placed on a normal skull in caudal and cranial view.*
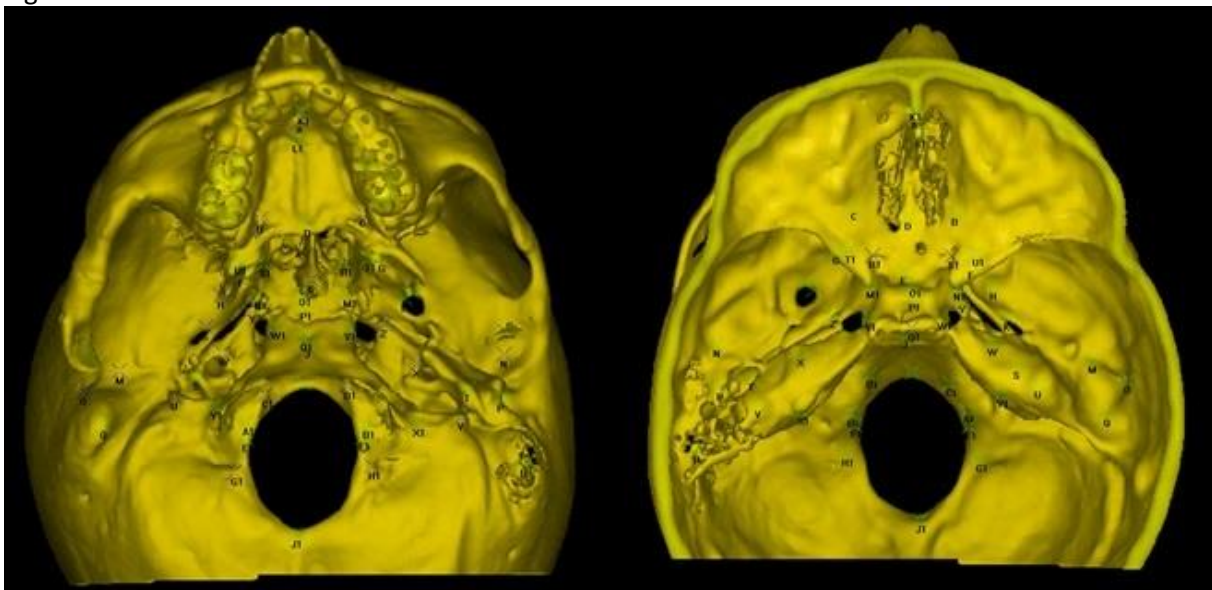
Figure 2

Figure 2 *The set of 51 landmarks placed on a CFM skull in caudal and cranial view*
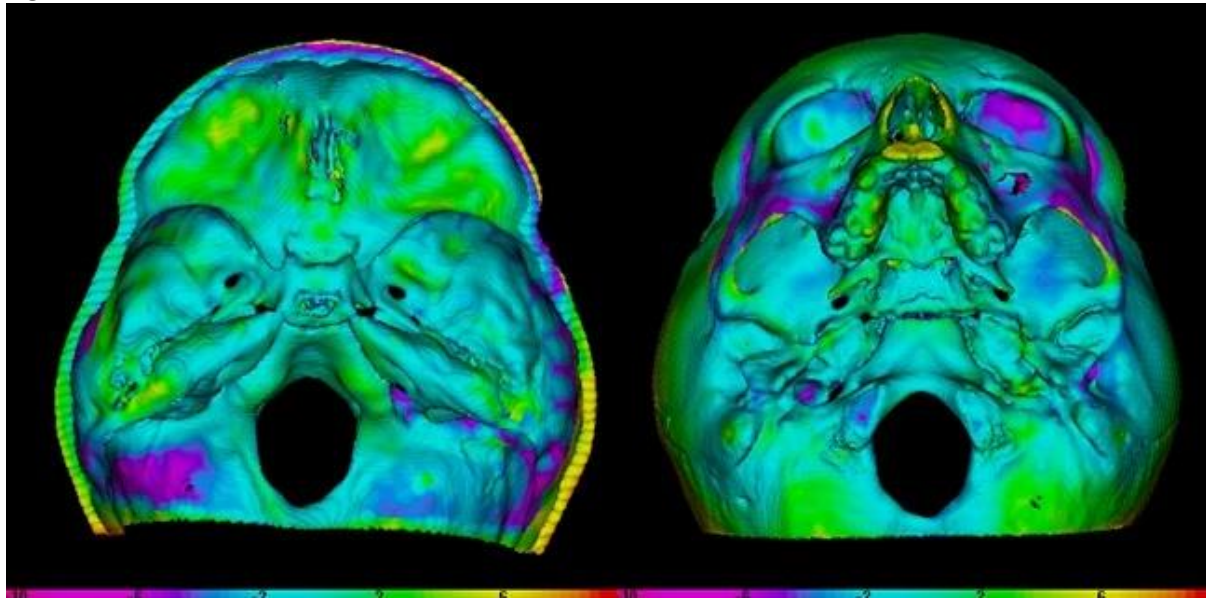
Figure 3

Figure 3 *The 10 mm range colour-coded map of the warped normal predicted skull being superimposed to its actual counterpart. The cranial and caudal views are shown. The green and light blue areas display sufficiently anatomical correspondence between the two scan.*
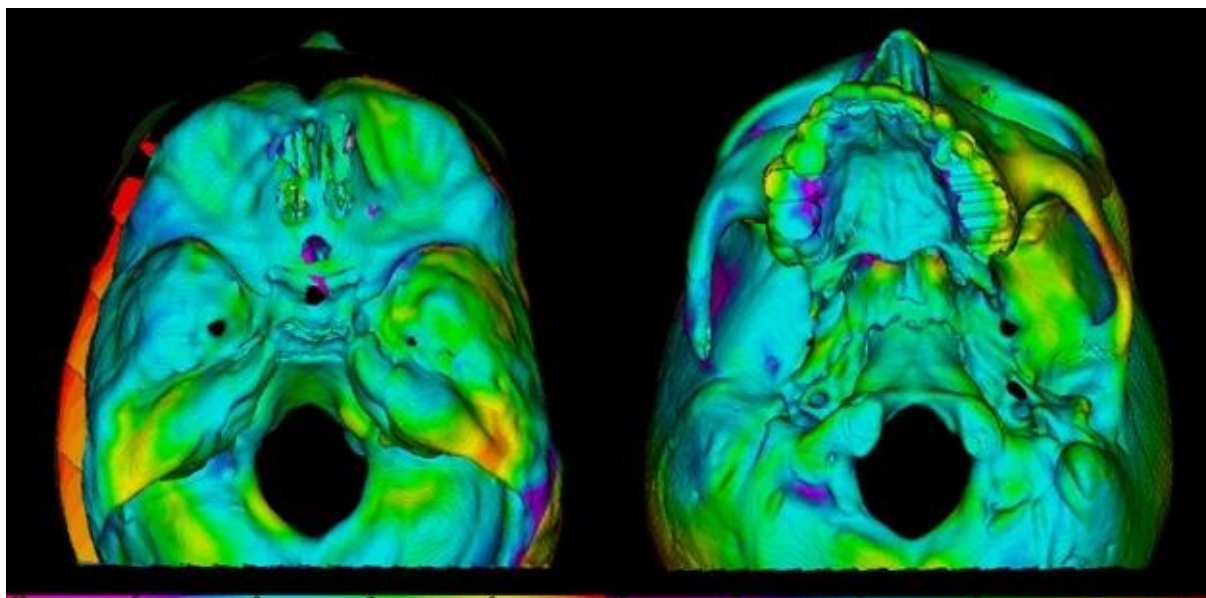
Figure 4

Figure 4 *The colour-code map in 10 mm range of the warped CFM predicted skull superimposed to its actual counterpart. The cranial and caudal views are shown. The green and light blue areas display sufficiently anatomical correspondence between the two scans by the chosen landmarks.*

LIST OF TABLES

TABLE 1. The distribution of age, gender, disorder and affected side of the CFM population

Age in years	Females	Males	CFM	Right	Left
7	1	1	2	1	1
8	2	1	3	1	2
9	0	0	0	0	0
10	2	3	5	3	2
11	2	1	3	3	0
12	0	0	0	0	0
Total	7	6	13	8	5

TABLE 2. The distribution in age and Pruzansky-Kaban classification of the

CFM population

Age in years	1	2A	2B	Total
7	0	2	0	2
8	0	3	0	3
9	0	0	0	0
10	1	1	3	5
11	0	1	2	3
12	0	0	0	0
Total	1	7	5	13

TABLE 3. Distribution of age and gender in the normal population

Age in years	Females	Males	Total
7	2	0	2
8	1	1	2
9	6	2	8
10	3	0	3
11	1	1	2
12	2	0	2
Total	15	4	19

TABLE 4. Set of 51 landmarks on the skull base used in this study. The fourth and fifth column represents the intra-observer reliability of each landmark.

Label	Landmark	Definition	SD normal	SD CFM
A	Incisive fossa	Most posteroinferior point	0.278	0.388
B	Right greater palatine foramen	Most anterior point of right greater palatine foramen	0.425	0.331
C	Left greater palatine foramen	Most anterior point of right greater palatine foramen	0.268	0.356
D	Posterior nasal spine	Most posterior point of posterior nasal spine.	0.52	0.855
E	Posterior border of vomer	Most posterior point of posterior border of vomer.	0.271	0.608
F	Right pterygoid hamulus	Most superior point of right pterygoid hamulus	0.29	0.22
G	Left pterygoid hamulus	Most superior point of right pterygoid hamulus	0.203	0.338
H	Right lateral pterygoid plate	Most superior point of the inferior part of the right lateral pterygoid plate	0.334	0.874
I	Left lateral pterygoid plate	Most superior point of the inferior part of the left lateral pterygoid plate	0.584	1.8

J	Pharyngeal tubercle	Most anteromedial point (V-shape) of pharyngeal tubercle.	0.997	0.717
K	Right foramen ovale	Most anteromedial inferior point of foramen ovale	0.558	0.268
L	Left foramen ovale	Most anteromedial inferior point of foramen ovale	0.619	0.753
M	Right mandibular fossa	The middle centre point of the right mandibular fossa	0.836	0.899
N	Left mandibular fossa	The middle centre point of the left mandibular fossa	1.014	1.359
O	Right external acoustic meatus	The centre of the highest point according to the frankfort horizontal; porion	0.469	0.893
P	Left external acoustic meatus	The centre of the highest point according to the frankfort horizontal; porion	0.381	2.332
Q	Right mastoid process	Point of maximum curvature of right mastoid process	1.331	0.591
R	Left mastoid process	Point of maximum curvature of left mastoid process	0.525	0.547
S	Right vaginal process of the tympanic portion; temporal bone	The most superior point of the right vaginal process; ensheated root of the styloid process.	0.638	2.248
T	Left vaginal process of the tympanic portion; temporal bone	The most superior point of the left vaginal process; ensheated root of the styloid process.	1.251	0.5
U	Right jugular foramen/jugular process	Most postero-superior point of right jugular foramen.	0.423	0.426
V	Left jugular foramen/ jugular process	Most postero-superior point of right jugular foramen.	0.648	0.408
W	Right carotid canal	Most anteroinferior point of right carotid canal.	0.503	0.824
X	Left carotid canal	Most anteroinferior point of left carotid canal.	0.658	0.974
Y	Right apex of petrous part of temporal bone	Most antero-superior point of apex.	0.276	0.367
Z	Left apex of petrous part of temporal bone	Most antero-superior point of apex.	0.267	0.397
A1	Right hypoglossal canal	Most postero-inferior point of hypoglossal canal.	0.86	0.855

B1	Left hypoglossal canal	Most postero-inferior point of left hypoglossal canal.	0.792	0.959
C1	Right occipital condyle	Most anteromedial point of right occipital condyle	1.01	0.741
D1	Left occipital condyle	Most anteromedial point of right occipital condyle	0.949	0.987
E1	Right occipital condyle	Most posteromedial point of the right occipital condyle	0.508	1.036
F1	Left occipital condyle	Most posteromedial point of of the left occipital condyle	0.676	1.252
G1	Right condylar canal posterior	Most posteromedial point of right condylar canal posterior	0.736	0.702
H1	Left condylar canal posterior	Most posteromedial point of left condylar canal posterior	0.539	0.73
I1	Foramen magnum	Most antero-medial point (basion)	0.499	0.573
JI	Foramen magnum	Most postero-medial point (opisthion)	0.572	0.603
K1	Foramen caecum	Most anteroinferior point of foramen caecum	1.106	1.412
L1	Crista galli	Top of crista Galli	0.589	0.595
M1	Left anterior clinoid process	Top of anterior clinoid process	0.47	0.633
N1	Right anterior clinoid process	Top of anterior clinoid process	0.482	0.564
O1	Tubercullum sellae	Most anterior point of tubercullum sella	0.825	0.428
P1	Pituitary fossa (sella turcica)	Point of greatest concavity of sella	0.728	0.612
Q1	Dorsum sellae	Most posterior point of sella	0.534	0.664
R1	Left optic canal	Most anteroinferior point of optic canal left	0.151	0.374
S1	Right optic canal	Most anteroinferior point of optic canal right	0.198	0.442
T1	Left foramen rotundum	Most anteroinferior point of foramen rotundum left	0.407	0.211
U1	Right foramen rotundum	Most anteroinferior point of foramen rotundum right	0.306	0.224
V1	Foramen lacerum left	Most medial inferior point of left foramen lacerum	0.46	0.724
W1	Foramen lacerum right	Most medial inferior point of right foramen lacerum	0.515	0.528

X1	Internal acoustic meatus left	Most posteroinferior point of internal acoustic meatus left	0.404	0.708
Y1	Internal acoustic meatus right	Most posteroinferior point of internal acoustic meatus right	0.436	0.287

TABLE 5. The mean and SD of cranial base angle (degrees)

	CFM (n=13)	Normal (N=19)	P-value
Foramen caecum; tuberculum sellae and to opisthion	2,964 ± 1,855	2,675 ± 2,150	0,7

TABLE 6. The mean and SD of cranial base length (mm)

	CFM (n=13)	Normal (N=19)	P-value
Foramen caecum to tuberculum sellae (anterior)	50,31 ± 1,996	40,07 ± 4,891	0,13
Tuberculum sellae to opisthion (posterior)	73,09 ± 3,137	76,38 ± 2,704	0,0035
Foramen caecum; tuberculum sellae and to opisthion	123,4 ± 3,072	124,5 ± 4,076	0,44

TABLE 7. The mean and SD lateral measurements (mm) comparison between the affected and unaffected side in the CFM group

	Affected	Unaffected	P-value
Hypoglossal canal to tuberculum sellae	51,04 ± 4,190	52,53 ± 4,150	0,022
Hypoglossal canal to basion	19,32 ± 2,326	19,73 ± 2,099	0,125
Internal acoustic meatus to tuberculum sellae	39,94 ± 3,961	44,41 ± 2,883	0,000*
Carotid canal to tuberculum sellae	38,17 ± 3,634	42,21 ± 2,778	0,000*
Optic canal to tuberculum sellae	14,04 ± 2,636	13,62 ± 2,718	0,417
Foramen ovale to tuberculum sellae	31,28 ± 3,566	32,08 ± 2,804	0,467
Foramen rotundum to tuberculum sellae	21,59 ± 1,798	22,40 ± 1,215	0,114
Mandibular fossa to tuberculum sellae	48,99 ± 4,542	51,21 ± 3,171	0,058
External acoustic meatus to tuberculum sellae	60,07 ± 5,017	56,23 ± 3,341	0,001
Mastoid process to tuberculum sellae	67,75 ± 4,587	75,05 ± 4,111	0,000*
Temporal bone to tuberculum sellae	48,50 ± 4,903	57,01 ± 2,593	0,000*
Mandibular fossa to mastoid process	23,27 ± 4,272	34,13 ± 2,437	0,000*
Mandibular fossa to temporal bone	13,46 ± 3,593	20,94 ± 2,183	0,000*
Temporal bone to mastoid process	19,92 ± 4,027	19,34 ± 2,942	0,599

* P-value under 0.001

TABLE 10. The mean lateral measurements and SD (mm) of the affected and unaffected side in the CFM group compared to the normal cohort

	Normal	Affected	P-value	Unaffected	P-value
Hypoglossal canal to tuberculum sellae	55,01 ± 2,414	51,04 ± 4,190	0.002	52,53 ± 4,150	0.039
Hypoglossal canal to basion	20,61 ± 5,091	19,32 ± 2,326	0.355	19,73 ± 2,099	0.524
Internal acoustic meatus to tuberculum sellae	45,65 ± 2,565	39,94 ± 3,961	0,000*	44,41 ± 2,883	0.237
Carotid canal to tuberculum sellae	44,07 ± 2,262	38,17 ± 3,634	0,000*	42,21 ± 2,778	0.054
Optic canal to tuberculum sellae	13,7 ± 2,316	14,04 ± 2,636	0.696	13,62 ± 2,718	0.925
Foramen ovale to tuberculum sellae	32,97 ± 2,413	31,28 ± 3,566	0.081	32,08 ± 2,804	0.357
Foramen rotundum to tuberculum sellae	22,29 ± 2,018	21,59 ± 1,798	0.277	22,40 ± 1,215	0.862
Mandibular fossa to tuberculum sellae	51,73 ± 1,897	48,99 ± 4,542	0.009	51,21 ± 3,171	0.598
External acoustic meatus to tuberculum sellae	56,53 ± 2,553	60,07 ± 5,017	0.005	56,23 ± 3,341	0.797
Mastoid process to tuberculum sellae	75,83 ± 3,951	67,75 ± 4,587	0,000*	75,05 ± 4,111	0.59
Temporal bone to tuberculum sellae	60,01 ± 2,935	48,50 ± 4,903	0,000*	57,01 ± 2,593	0.012
Mandibular fossa to mastoid process	33,03 ± 3,726	23,27 ± 4,272	0,000*	34,13 ± 2,437	0.381
Mandibular fossa to temporal bone	22,05 ± 2,634	13,46 ± 3,593	0,000*	20,94 ± 2,183	0.248
Temporal bone to mastoid process	17,88 ± 2,033	19,92 ± 4,027	0.034	19,34 ± 2,942	0.126

* P-value under 0.001